particles

MDPI

Article

Cross-Sections of Neutral-Current Neutrino Scattering on ^{94,96}Mo Isotopes

T. S. Kosmas [1], R. Sahu [2,*] and V. K. B. Kota [3]

[1] Division of Theoretical Physics, University of Ioannina, GR 45110 Ioannina, Greece; hkosmas@uoi.gr
[2] National Institute of Science and Technology, Palur Hills, Berhampur 761008, India
[3] Physical Research Laboratory, Ahmedabad 380009, India; vkbkota@prl.res.in
* Correspondence: rankasahu@gmail.com

Abstract: In our recent publications, we presented neutral-current ν–nucleus cross-sections for the coherent and incoherent channels for some stable Mo isotopes, assuming a Mo detector medium, within the context of the deformed shell model. In these predictions, however, we have not included the contributions in the cross-sections stemming from the stable ^{94,96}Mo isotopes (abundance of ^{94}Mo 9.12% and of ^{96}Mo 16.50%). The purpose of the present work is to perform detailed calculations of ν–^{94,96}Mo scattering cross-sections, for a given energy E_ν of the incoming neutrino, for coherent and incoherent processes. In many situations, the E_ν values range from 15 to 30 MeV, and in the present work, we used $E_\nu = 15$ MeV. Mo as a detector material has been employed by the MOON neutrino and double-beta decay experiments and also from the NEMO neutrinoless double-beta decay experiment. For our cross-section calculations, we utilize the Donnelly–Walecka multipole decomposition method in which the ν–nucleus cross-sections are given as a function of the excitation energy of the target nucleus. Because only the coherent cross-section is measured by current experiments, it is worth estimating what portion of the total cross-section represents the measured coherent rate. This requires the knowledge of the incoherent cross-section, which is also calculated in the present work.

Keywords: electroweak neutral-current processes; neutrino–nucleus scattering cross-sections; deformed shell model; Donnelly–Walecka decomposition method; coherent neutrino–nucleus scattering; CEνNS experiments; incoherent neutrino–nucleus scattering; state-by-state calculations; ^{94,96,98,100}Mo

Citation: Kosmas, T.S.; Sahu, R.; Kota, V.K.B. Cross-Sections of Neutral-Current Neutrino Scattering on ^{94,96}Mo Isotopes. *Particles* **2024**, *7*, 887–898. https://doi.org/10.3390/particles7040053

Academic Editor: Armen Sedrakian

Received: 28 August 2024
Revised: 24 September 2024
Accepted: 27 September 2024
Published: 4 October 2024

1. Introduction

As is well known, the neutral-current neutrino–nucleus scattering cross-sections are about two to four orders of magnitude larger than that of the charged-current neutrino-nucleus process [1–5]. However, due to the different signal to the detector in these two processes, the neutral-current neutrino–nucleus scattering has been measured only recently, about half a century after its first prediction by Freedman [1], with the COHERENT experiment at the SNS neutron spallation source in Oak Ridge, USA [6–8]. It should be noted that in the case of the neutral-current neutrino–nucleus scattering, the coherent elastic ν–nucleus scattering (CEνNS) process is possible in which the signal to the detector is the recoil energy released on the nuclear target.

This implies that the observation of CEνNS is possible by employing, instead of multi-ton neutrino detectors, much smaller neutrino detection devices with the total detector mass of the kg scale. Thus, the weak neutral current process is difficult to detect due to the very low momentum transfer of the scattering process, which leads to recoil energies of the order of only a few keV. This was the main reason why this process has been only recently been observed [6,7]. Afterwards, this research topic started growing up from experimental perspectives [9–17] as well as from a theoretical and phenomenological viewpoint; see [5,18–25] and references therein.

Nowadays, new experiments have been designed, like the NUCLEUS experiment at TU Munich, Germany, aiming at the first measurement of CEνNS in a nuclear reactor using reactor neutrinos (there, the neutrino fluxes have high intensity) at the, relatively, very low energy range (up to 10 MeV) of the nuclear power plant in Chooz, France. The NUCLEUS experiment is going to utilize dedicated cryogenic detectors with nuclear recoil energy thresholds estimated to be around 20 eV. This is the lowest used in the topic of CEνNS. At present, the NUCLEUS setup is in the stage of building (in the shallow underground laboratory at TUM) and commissioning, and it is expected that the experiment will be moved to France next year. The scientific potential with several technological details of this experiment can be found, e.g., in [15,26].

On the other hand, the Conus experiment, at the Brokdorf Nuclear Power Plant, near Hamburg, Germany, studies CEνNS in four spectrometers of about 1 kg germanium each by utilizing low ionization energy thresholds of $E_{rec} = 210$ eV. The detectors were operated inside an optimized shield (the reactor antineutrino flux reaches a value of up to $\Phi = 2.3 \times 10^{13}/\text{cm}^2$ s). In the final phase of data collection at this site, the constraints on the neutrino interaction rate were improved by an order of magnitude as compared to the previous Conus analysis [11,27].

The main aim of our present work is to compute reliable predictions for both coherent and incoherent neutrino–nucleus scattering cross-sections starting from the differential cross-section formalism and employing the Donnelly–Walecka multipole decomposition method. This method provides neutrino–nucleus scattering cross-sections as a function of the excitation energy of the target nucleus (or equivalently as a function of the outgoing neutrino energy). For the realistic estimation of the relevant nuclear matrix elements, we utilize the deformed shell model (DSM) [28], which has up to now been employed for similar reliable predictions in several electroweak nuclear processes; see [18,19,28] and references therein. We mention that besides DSM, many other nuclear models are employed for neutrino–nucleus scattering cross-sections calculations. These include Fermi gas models [3], Continuum random phase approximation (CRPA) [20], quasiparticle random phase approximation (QRPA) [21,23], microscopic quasiparticle–phonon model (MQPM) [22], shell model [24] and Nilsson model [25]. In particular, for Mo isotopes, results from QRPA are available in the literature [21,23], and they are compared with the present DSM results in Section 5.

It is worth noting that up to now, a Mo detector has not been employed in CEνNS experiments. However, due to its promising experimental criteria, this detector medium has been proposed for appreciably sensitive experiments as neutrino masses, double-beta-decay and dark matter in the MOON experiment [29,30] as well as in the NEMO neutrinoless double-beta decay experiments [31].

The detector material employed in neutrino experiments is not enriched, which means that in the proposed Mo detector, all stable Mo isotopes are present. On the other hand, the CEνNS cross-sections are strongly dependent on the neutron number of the detector nucleus. This means that reliable predictions for the Mo CEνNS detector must take into account all stable Mo isotopes. In our recent work [19], we have not included neutral-current ν–nucleus cross-sections for ^{94,96}Mo isotopes. The purpose of our present paper is to perform detailed deformed shell model cross-sections calculations on ν-^{94,96}Mo coherent and incoherent scattering. These cross-sections depend on the given energy E_ν of the incoming neutrino. In many neutrino sources (solar neutrinos, pion-decay at rest neutrinos, low-energy supernova neutrinos, etc.) the neutrino–energy range reaches up to E_ν = 15–30 MeV [7,32–34]. In this work, we consider a typical incoming neutrino energy $E_\nu = 15$ MeV.

The material in the rest of the paper is organized as follows. In Section 2, a brief description of the related coherent and incoherent cross-section calculation formalism is presented. Then, (in Section 3), the main features of the deformed shell model are shortly described. In Section 4, we present the low-lying collective bands in ^{94,96}Mo isotopes created within the assumptions of the deformed shell model. These bands are used in the

state-by-state calculations of the differential cross-sections, which have been performed in our present work. Subsequently, (in Section 5), we discuss rather extensively the obtained results for the ^{94,96}Mo isotopes that are contents of a non-enriched Mo detector material which may be employed in CEνNS experiments. We remind that such a detector has been employed previously for appreciably sensitive (neutrino, double-beta decay and dark matter) experiments. Finally (in Section 6), we summarize the extracted conclusions and mention future extensions of this work.

2. Brief Description of the Related Formalism

The formulation, adopted in this paper, that provides the neutral current ν–nucleus scattering differential cross-sections was given earlier by Donnelly et al.; see [35,36] and also by Tsakstara and Kosmas [4,37]. For completeness, a few important steps are described below. In the low energy region, the weak interaction neutrino–nucleus Hamiltonian $\hat{H}_w$ in the effective current-current form is

$$\hat{H}_w = -\frac{G}{\sqrt{2}} \int d^3x \, \hat{j}_\mu^{lept}(\mathbf{x}) \hat{\mathcal{J}}^\mu(\mathbf{x}) \, . \tag{1}$$

Here, $\hat{j}_\mu^{lept}$ and $\hat{\mathcal{J}}^\mu$ denote the leptonic and hadronic currents, respectively, and G is the Fermi weak coupling constant. Now, applying a multipole analysis as described in detail in [4,35–37], a double differential cross-section for scattering from the initial state (normally this is the ground state) $\mid i\rangle \equiv \mid J_i^\pi M_i\rangle$ to the final state (ground state or an excited state) $\mid f\rangle \equiv \mid J_f^\pi M_f\rangle$ is given by

$$\frac{d^2\sigma_{i\to f}}{d\Omega d\omega}(\phi,\theta,\omega,\epsilon_i) = \delta(E_f - E_i - \omega) \frac{2G^2\epsilon_f^2 \cos^2(\theta/2)}{\pi(2J_i+1)} [C_V + C_A \mp C_{VA}] \, . \tag{2}$$

The δ-function above ensures energy conservation, and thus, the excitation energy ω of the nucleus is

$$\omega = E_f - E_i = \epsilon_i - \epsilon_f \, , \tag{3}$$

where E_i and E_f are the energies of the initial and final states of the nucleus involved and ϵ_i and ϵ_f are the energies of the incoming and outgoing neutrino. In Equation (2), the $(-)$ sign corresponds to the scattering of the neutrinos and the $(+)$ corresponds to the scattering of the antineutrinos.

The C_V and C_A terms in Equation (2) include a summation over the contributions coming from the polar-vector and axial-vector multipole operators, respectively, and they are

$$\begin{aligned} C_V &= \sum_{J=0}^{\infty} \mid \langle J_f \mid\mid \hat{M}_J(q) + \frac{\omega}{q}\hat{L}_J(q) \mid\mid J_i\rangle \mid^2 \\ &+ \sum_{J=1}^{\infty} \left(-\frac{q_\mu^2}{2q^2} + \tan^2\frac{\theta}{2} \right) \left[\mid \langle J_f \mid\mid \hat{T}_J^{mag}(q) \mid\mid J_i\rangle \mid^2 + \mid \langle J_f \mid\mid \hat{T}_J^{el}(q) \mid\mid J_i\rangle \mid^2 \right] . \end{aligned} \tag{4}$$

$$\begin{aligned} C_A &= \sum_{J=0}^{\infty} \mid \langle J_f \mid\mid \hat{M}_J^5(q) + \frac{\omega}{q}\hat{L}_J^5(q) \mid\mid J_i\rangle \mid^2 \\ &+ \sum_{J=1}^{\infty} \left(-\frac{q_\mu^2}{2q^2} + \tan^2\frac{\theta}{2} \right) \left[\mid \langle J_f \mid\mid \hat{T}_J^{mag5}(q) \mid\mid J_i\rangle \mid^2 + \mid \langle J_f \mid\mid \hat{T}_J^{el5}(q) \mid\mid J_i\rangle \mid^2 \right] . \end{aligned} \tag{5}$$

The C_{VA} term in Equation (2) is the interference term, and it involves the product of transverse polar-vector and transverse axial-vector matrix elements as

$$\begin{aligned} C_{VA} &= 2\tan\frac{\theta}{2}\left(-\frac{q_\mu^2}{q^2}+\tan^2\frac{\theta}{2}\right)^{1/2} \\ &\times\sum_{J=1}^{\infty} Re\langle J_f \mid\mid \hat{\mathcal{T}}_J^{mag}(q) \mid\mid J_i\rangle\langle J_f \mid\mid \hat{\mathcal{T}}_J^{el}(q) \mid\mid J_i\rangle^* . \end{aligned} \tag{6}$$

For normal parity transitions, $\hat{\mathcal{T}}_J^{el} = \hat{T}_J^{el}$ and $\hat{\mathcal{T}}_J^{mag} = \hat{T}_J^{mag5}$, while for abnormal parity ones, $\hat{\mathcal{T}}_J^{el} = \hat{T}_J^{el5}$ and $\hat{\mathcal{T}}_J^{mag} = \hat{T}_J^{mag}$. The definitions of the eight multipole operators $\hat{M}_J$, $\hat{L}_J$, $\hat{T}_J^{el}$, $\hat{T}_J^{mag}$, $\hat{M}_J^5$, $\hat{L}_J^5$, $\hat{T}_J^{el5}$ and $\hat{T}_J^{mag5}$ and other details are given in [19,38] and summarized below. Going further, the square of the four-momentum transfer q_μ^2 and the magnitude of the three-momentum transfer $q \equiv \mid \mathbf{q} \mid$ [they appear in Equations (4)–(6)] can be written in terms of the laboratory scattering angle θ and the neutrino energies $\epsilon_i = \epsilon_\nu$ and $\epsilon_f = (\epsilon_i - \omega)$ giving

$$\begin{aligned} q_\mu^2 &= -4\epsilon_i(\epsilon_i-\omega)\sin^2(\theta/2) \\ q &\equiv \mid \mathbf{q} \mid = \left[\omega^2 + 4\epsilon_i(\epsilon_i-\omega)\sin^2(\theta/2)\right]^{1/2} . \end{aligned} \tag{7}$$

In addition to the above, also needed are the weak nucleon form factors F_i^Z, $i = 1, 2$ and the neutral current axial-vector form factor F_A^Z for protons (p) and neutrons (n). These enter in the definition of the eight multipole operators mentioned above as (neglecting the pseudo-scalar form factors),

$$\begin{aligned} &\hat{M}_{JM}^{Coul}(q\mathbf{r}) = F_1^Z \hat{M}_M^J(q\mathbf{r}), \qquad \hat{L}_{JM}(q\mathbf{r}) = \frac{q_0}{q}\hat{M}_{JM}^{Coul}(q\mathbf{r}), \\ &\hat{T}_{JM}^{el}(q\mathbf{r}) = \frac{q}{M}\left[F_1^Z\Delta_M'^J(q\mathbf{r}) + \frac{1}{2}(F_1^Z + 2MF_2^Z)\Sigma_M^J(q\mathbf{r})\right], \\ &i\hat{T}_{JM}^{mag}(q\mathbf{r}) = \frac{q}{M}\left[F_1^Z\Delta_M^J(q\mathbf{r}) - \frac{1}{2}(F_1^Z + 2MF_2^Z)\Sigma_M'^J(q\mathbf{r})\right], \\ &i\hat{M}_{JM}^5(q\mathbf{r}) = \frac{q}{M}\left[F_A^Z\Omega_M^J(q\mathbf{r}) + \frac{1}{2}F_A^Z\Sigma_M''^J(q\mathbf{r})\right], \\ &-i\hat{L}_{JM}^5(q\mathbf{r}) = F_A^Z\Sigma_M''^J(q\mathbf{r}), \\ &-i\hat{T}_{JM}^{el5}(q\mathbf{r}) = F_A^Z\Sigma_M'^J(q\mathbf{r}), \\ &\hat{T}_{JM}^{mag5}(q\mathbf{r}) = F_A^Z\Sigma_M^J(q\mathbf{r}) . \end{aligned} \tag{8}$$

Here, the first three and last multipole operators have normal parity, $\pi = (-)^J$, while others have abnormal parity, $\pi = (-)^{J+1}$. The explicit forms of the seven operators M_{JM}^{Coul}, Δ_M^J, $\Delta_M'^J$, Ω_M^J, Σ_M^J, $\Sigma_M'^J$ and $\Sigma_M''^J$ are given in [36,38].

It is important to note that the superscript Z in the form factors refers to the processes with Z-boson exchange. Firstly, the $F_{1,2}^Z$ for protons and neutrons are expressed in terms of the well-known charge and electromagnetic form factors for proton $F_{1,2}^p$ and neutron $F_{1,2}^n$, using CVC theory, as [36]

$$\begin{aligned} F_{1,2}^Z(p) &= \left(\tfrac{1}{2} - \sin^2\theta_W\right)F_{1,2}^p - \sin^2\theta_W F_{1,2}^p , \\ F_{1,2}^Z(n) &= -\left(\tfrac{1}{2} - \sin^2\theta_W\right)F_{1,2}^n - \sin^2\theta_W F_{1,2}^n . \end{aligned} \tag{9}$$

Here, θ_W is the Weinberg angle and $\sin^2\theta_W = 0.2325$. The Dirac and Pauli form factors F_1 and F_2 for the proton and neutron are given in Ref. [39], and they are $F_1^p = 1$ and $F_2^p = k_p$, $F_1^n = 0$ and $F_2^n = k_n$. The anomalous magnetic moments k_p and k_n are related to the magnetic moments of the proton and neutron,

$$k_p = \mu_p - 1, \quad k_n = \mu_n, \qquad \mu_p = 2.7928 \text{ nm}, \quad \mu_n = -1.9130 \text{ nm} . \tag{10}$$

The neutral current axial-vector form factor for protons $F_A^Z(p) = \frac{1}{2}F_A(q_\mu^2)$ and for neutrons $F_A^Z(n) = -\frac{1}{2}F_A(q_\mu^2)$. In our calculations, we employ the static value $F_A(q_\mu^2) = g_A = -1.258$, and this follows from the dipole ansatz. Also, we take into account the quenching effect on the axial vector form factor g_A as described in Section 5 ahead.

Before going further, let us mention that for evaluating the reduced matrix elements in Equations (4)–(6), all we need are the reduced matrix elements of the seven operators M_{JM}^{Coul}, Δ_M^J, $\Delta_M'^J$, Ω_M^J, Σ_M^J, $\Sigma_M'^J$ and $\Sigma_M''^J$ appearing in Equation (8). These reduced matrix elements are evaluated using the nuclear eigenfuctions generated using a deformed shell model, and now we will turn to a brief description of DSM, which is a nuclear structure model.

3. Deformed Shell Model

The method involved in making nuclear structure calculations using a deformed shell model (DSM) (DSM was introduced in 1971) and its various applications are described in a book on DSM [28] and also in many publications. In the mass region A = 60–100 in particular, the DSM is shown to be quite successful in describing spectroscopic properties like band crossings, shape coexistence, electromagnetic transition probabilities, isospin $T = 0$ and $T = 1$ bands in N = Z odd–odd nuclei, and so on. Going beyond spectroscopy, more recently, DSM has also been employed quite successfully for obtaining nuclear structure factors needed for a variety of weak processes, and these include (i) two-neutrino and neutrinoless double-beta decay, including positron double-beta decay; (ii) $\mu \rightarrow e$ conversion in the field of the nucleus; (iii) event rates for WIMP–nucleus scattering; and (iv) coherent and incoherent event rates for the neutrino–nucleus scattering. See [18,19,28] and references therein for various papers on these topics.

In DSM, just as in the spherical shell model, for a given nucleus, one starts with a model space (this defines the number of valence protons and valence neutrons and the core) consisting of a given set of single particle (sp) orbitals, the associated sp energies (spe) and an effective two-body Hamiltonian with the associated two-body matrix elements (TBME). Then, the steps involved in the calculations are as follows. (i) Firstly, the lowest energy prolate and oblate intrinsic states are obtained by solving the axially symmetric Hartree–Fock (HF) single-particle equation self-consistently (see Figures 1 and 3 ahead). (ii) By making particle–hole excitations over the lowest intrinsic states, excited intrinsic states (configurations) are obtained. (iii) As the intrinsic states $\chi_K(\eta)$ will not have definite angular momenta, good angular momentum states are projected from the $\chi_K(\eta)$ states, and this can be written in the form

$$\psi_{MK}^J(\eta) = \frac{2J+1}{8\pi^2\sqrt{N_{JK}}} \int d\Omega D_{MK}^{J^*}(\Omega) R(\Omega) |\chi_K(\eta)\rangle \tag{11}$$

where N_{JK} is the normalization constant given by

$$N_{JK} = \frac{2J+1}{2} \int_0^\pi d\beta \sin\beta d_{KK}^J(\beta) \langle \chi_K(\eta)| e^{-i\beta J_y} |\chi_K(\eta)\rangle \ . \tag{12}$$

In Equation (11), Ω represents the Euler angles (α, β, γ), $R(\Omega)$ which is equal to $\exp(-i\alpha J_z)$ $\exp(-i\beta J_y)$ $\exp(-i\gamma J_z)$ represents the general rotation operator. (iv) The good angular momentum states $\psi_{MK}^J(\eta)$ will not be, in general, orthogonal to each other, and hence they are orthonormalized, and then band mixing calculations are performed. The resulting eigenfunctions following the steps (i)–(iv) are of the form

$$|\Phi_M^J(\eta)\rangle \ = \ \sum_{K,\alpha} S_{K\eta}^J(\alpha) |\psi_{MK}^J(\alpha)\rangle \, . \tag{13}$$

The reduced matrix elements occurring in Equations (4)–(6) are evaluated using the DSM wave function $\Phi_M^J(\eta)$ defined in Equation (13). As a part of this, one has to first calculate the reduced matrix elements of the seven operators M_{JM}^{Coul}, Δ_M^J, $\Delta_M'^J$, Ω_M^J, Σ_M^J, $\Sigma_M'^J$ and

Σ''^{J}_{M} appearing in Equation (8) in the single particle space (in proton orbits and in neutron orbits), as these are all one-body operators. For details of the one-particle matrix elements and how to use these with DSM wave functions generated for the Mo isotopes, see [28,38].

4. The Low-Lying Deformed Shell Model Collective Bands in ^{94,96}Mo Isotopes

In order to generate wave functions for ^{94,96}Mo isotopes, we carry out the DSM calculation as described above using the effective interaction *GWBXG* with the ^{66}Ni closed core. The effective interaction has been constructed with different interactions as described in detail in refs. [40,41]. Dey et al [40] have successfully used this effective interaction within the spherical shell model to analyze the experimental data in ^{90}Zr. The active proton sp orbitals in this effective interaction are $0f_{5/2}$, $1p_{3/2}$, $1p_{1/2}$, and $0g_{9/2}$ with spe -5.322, -6.144, -3.941, and -1.250 MeV. For the neutrons, the active sp orbitals are $1p_{1/2}$, $0g_{9/2}$, $0g_{7/2}$, $1d_{5/2}$, $1d_{3/2}$, and $2s_{1/2}$. The spe for the first five sp orbitals are taken to be -0.696, -2.597, 5.159, 1.830, and 4.261 MeV, respectively, as in the *GWBXG* interaction. Just as seen in our previous study involving ^{98,100}Mo [19], it is found also in the present calculations that the $2s_{1/2}$ orbital produces low-lying large deformed solutions. However, Mo isotopes are known to be weakly deformed. As a result, as in [19], the effect of this orbital is eliminated by taking the corresponding neutron spe at a high value.

Using the above model space and the effective interaction, we first carried out, for each nucleus, an axially symmetric HF calculation by solving the HF equation self-consistently for ^{94}Mo. The lowest energy prolate and oblate HF sp spectra are shown in Figure 1. It is seen in the figure that the prolate and oblate solutions are almost degenerate with the oblate solution lower by about 1 MeV. The intrinsic quadrupole moment is small for both the solutions, indicating that this nucleus is weakly deformed. Then, we perform particle–hole excitations across the proton and neutron Fermi surfaces and generate excited intrinsic configurations. For positive parity, we have considered 32 intrinsic states (17 prolate and 15 oblate) having $K = 0^+$, 1^+ and 2^+. Similarly, we have considered 25 negative parity intrinsic states (13 prolate and 12 oblate) with particle–hole excitations. Good angular momentum states are projected from each of these intrinsic states, and then band mixing is performed separately for positive parity states and negative parity states. Further, states having similar electromagnetic properties are classified into one band. The calculated ground band and a few low-lying levels are compared with the experiments in Figure 2 for this nucleus. We find that the ground band is quite nicely reproduced within our model. Experimentally, an excited 0^+ level has been observed at 1.742 MeV. Our calculated first excited 0^+ is at 2.612 MeV, which is about 1 MeV higher and hence can not be compared with the above 0^+ state. However, there is another 0^+ state experimentally at 2.781 MeV, which can be compared with our calculated 0^+ state. The observed first 3^- level at 2.534 MeV agrees quite well with our calculated 3^- state, which is at 2.550 MeV. Since the 1^+ state plays an important role in neutrino–nucleus scattering, we have predicted such a state at 2.415 MeV. In addition, there are two low-lying 2^+ states and a 4^+state. These levels are calculated and presented in the figure.

Similarly for ^{96}Mo, the lowest energy prolate and oblate intrinsic solutions are obtained by solving the HF single particle equation self consistently, and the corresponding sp spectra are shown in Figure 3. It is seen from the figure that the prolate and oblate solutions are almost degenerate, differing only by 0.37 MeV, oblate being lower. The excited intrinsic states are obtained by performing particle–hole excitations across the proton and neutron Fermi surfaces. For positive parity, we have considered 33 intrinsic states with 16 prolate and 17 oblate. We have also considered 24 negative parity intrinsic states. Using these intrinsic states, for each parity separately, we carried out angular momentum projection, orthonormalization and band mixing. Then, the resulting states having a similar structure and, thus, similar electromagnetic properties are classified into the same band. For ^{96}Mo, not many collective bands have been observed. In Figure 4, we compare the calculated ground band with the experimentally observed band, and we see that the agreement is reasonable. As in ^{94}Mo, we have compared the observed low-lying levels with an

experiment for this nucleus. The calculated first excited 0^+ level is above 1 MeV, which is higher compared to the experiment. Hence, this level should be compared with the observed 0^+ level at 2.623 MeV. Experimentally, there are two low-lying 3^- levels. Our calculated 3^- level is at 3.057 MeV, which should be compared with the second 3^- level. In this nucleus also, there are two low-lying 2^+ levels and a 4^+. These levels are presented in the figure.

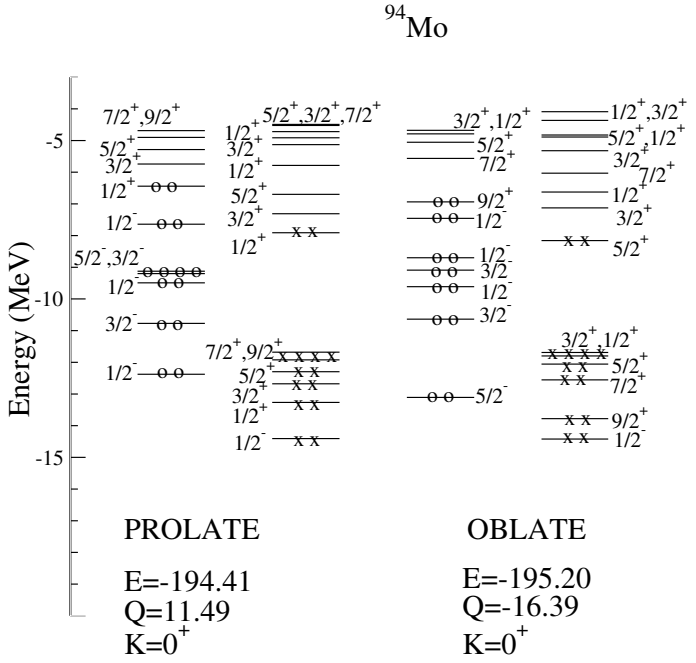

Figure 1. HF single-particle spectra for ^{94}Mo corresponding to lowest energy prolate and oblate configurations. In the figure, circles represent protons and crosses represent neutrons. The HF energy E in MeV, mass quadrupole moment Q in units of the square of the oscillator length parameter and the total azimuthal quantum number K are given in the figure.

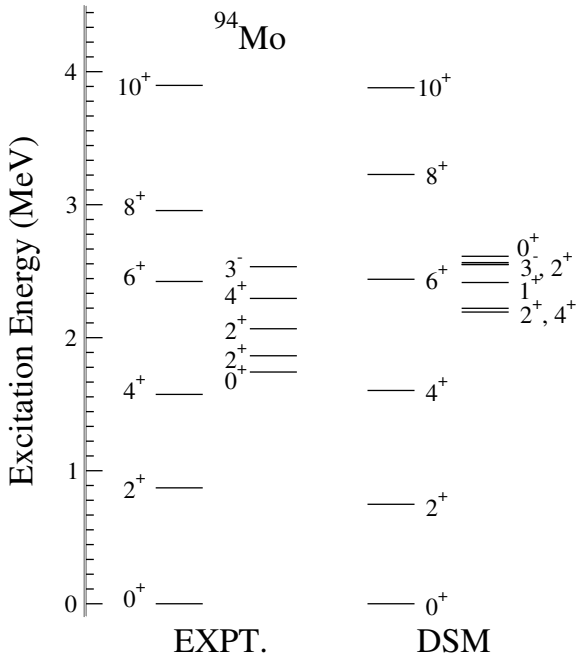

Figure 2. The ground band and a few other low-lying levels observed in ^{94}Mo are compared with the DSM predictions. The experimental data are taken from [42].

Before closing this section, we mention that the DSM results for ^{94,96}Mo for spectroscopic properties such as $B(E2)$ values and magnetic moments will be presented elsewhere.

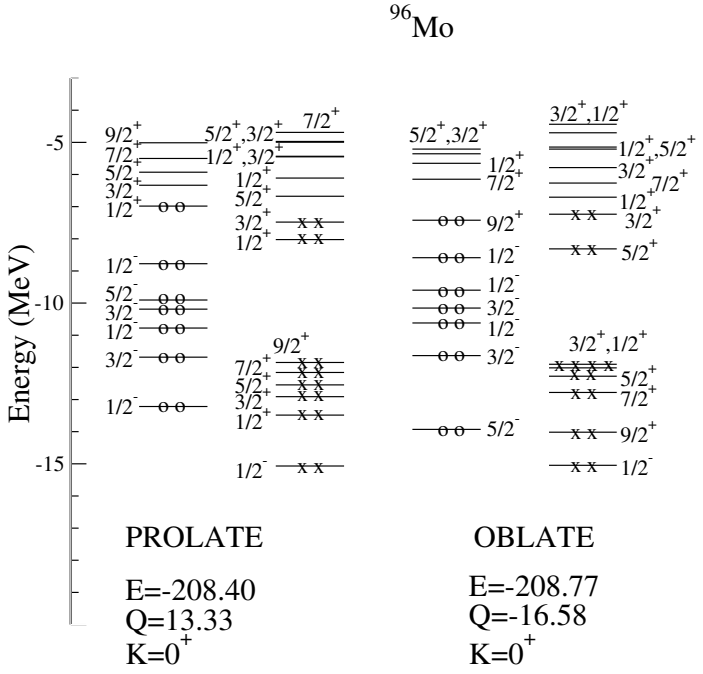

Figure 3. HF single-particle spectra for ^{96}Mo corresponding to lowest energy prolate and oblate configurations. In the figure, circles represent protons and crosses represent neutrons. The HF energy E in MeV, mass quadrupole moment Q in units of the square of the oscillator length parameter and the total azimuthal quantum number K are given in the figure.

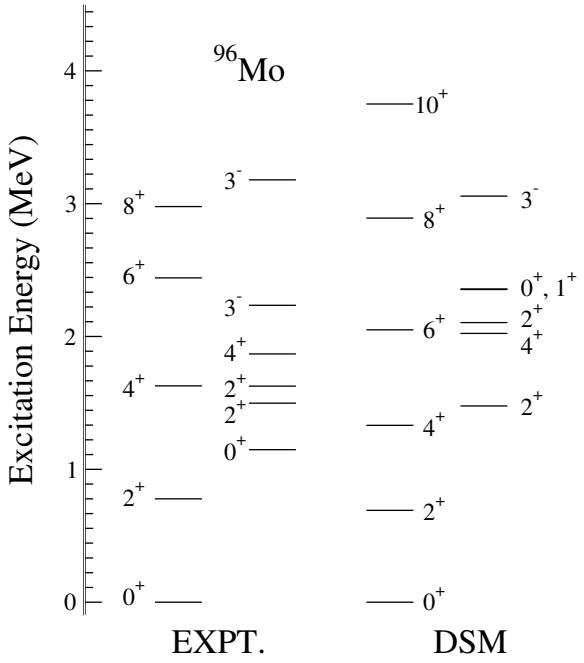

Figure 4. The ground band and a few other low-lying levels observed in ^{96}Mo are compared with the DSM predictions. The experimental data are taken from [42].

5. Results and Discussion

Employing the formulation described in Section 2 and the DSM wave functions (see Sections 3 and 4), we have calculated the coherent (ground state 0^+ to ground state 0^+ cross-

section, i.e., the elastic scattering cross-section) as well as the incoherent (ground state 0^+ to each excited J^π states) cross-sections for the Mo isotopes with A = 94, 96. They are evaluated using the proper transition matrix elements, defining C_V, C_A and C_{VA} (Equations (4)–(6)), and connecting the ground 0^+ state to various excited J^π states through the use of the DSM wave function $\Phi^J_M(\eta)$ defined in Equation (13). For the coherent case, J^π is the ground 0^+. The incoming neutrino energy is assumed to be $\epsilon_\nu = 15$ MeV. As in our previous publication [19], we use a quenching factor of 0.35. The coherent differential cross-section for ^{94}Mo comes out to be 1165, whereas for ^{96}Mo, it is 1338.5. The basic operator M^J contributes to this cross-section. For ^{94,96}Mo, the incoherent differential cross-sections as a function of their excitation energies are given in Figures 5 and 6. As can be seen in these figures, the most dominant contributions are the multipolarities $J = 1^+$ (represented by red), $J = 2^+$ (represented by blue), $J = 1^-$ (represented by black), and $J = 2^-$ (represented by cyan). We find that the basic operators Σ'^J, Σ''^J, Δ^J and Ω^J contribute to the multipolarities $J = 1^+$ and $J = 2^-$. Similarly, for multipolarity $J = 2^+$, the contribution comes from the basic operators M^J, Σ^J and Δ'^J. For ^{94}Mo, DSM predicts thirteen 1^+ states. The contribution of the 1^+ multipole at ω = 2.415 MeV is the largest and has the value 58. For ^{96}Mo, there are twelve 1^+ states and the contribution of this multipole at ω = 3.165 MeV is the largest.

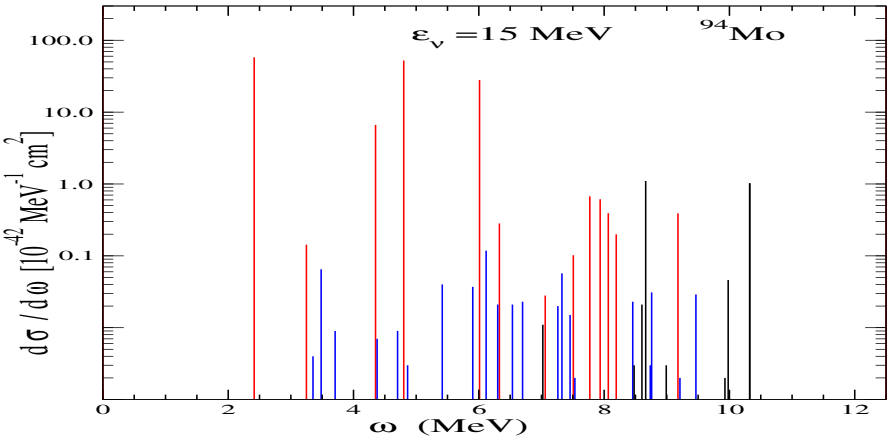

Figure 5. The differential cross-section as a function of the excitation energy ω for ^{94}Mo at incoming neutrino energy $\epsilon_\nu = 15$ MeV for different excited states. The contribution of the excitation to $J = 1^+$ state is represented by red, to $J = 2^+$ by blue, to $J = 1^-$ by black, and to $J = 2^-$ by cyan.

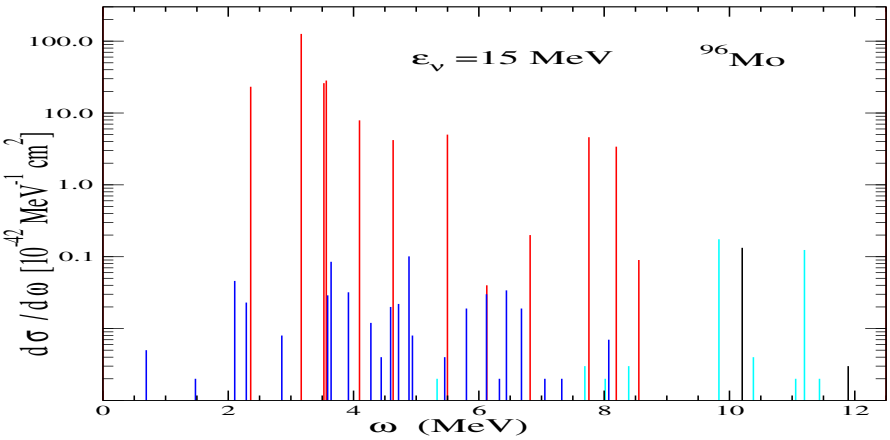

Figure 6. The differential cross-section as a function of the excitation energy ω for ^{96}Mo at incoming neutrino energy $\epsilon_\nu = 15$ MeV for different excited states. Figure is generated with the data taken from ref. [18]. The contribution of the excitation to the $J = 1^+$ state is represented by blue, to $J = 2^+$ by red, to $J = 1^-$ by cyan, and to $J = 2^-$ by black.

In Table 1, we have tabulated the coherent, incoherent and total differential cross-sections obtained from our present calculation for each of the detector isotopes, ^{94,96,98,100}Mo. In addition, the ratio of the measured coherent cross-section over the total cross-section is also listed in this table. Comparing the results in Table 1 with those from QRPA calculations presented in [21,23], it is seen that the QRPA results for incoherent cross-sections are much smaller than those from present DSM results. Similarly, the coherent results from QRPA are larger than the DSM results. In addition, as seen from Table 1, the coherent cross-sections show a very good correlation to the square of the neutron number ($\sim N^2$) of each isotope. On the other hand, the structures of the low-lying excited states appear to govern the incoherent cross-sections, as seen from the comparison of the QRPA results in [21,23], with those in Table 1. It is important to mention that QRPA takes into account pairing correlations much better, and DSM takes into account deformation effects much better. Obviously, possible measurements of the coherent cross-section by the ongoing or designed CEνNS experiments (see the discussion in the Introduction) with the use of Mo as detector medium will offer the possibility to compare the cross-sections of Table 1 with the experimental results.

It is worth noting that since at present, incoherent cross-section measurements are extremely difficult, on the basis of our predictions, we estimate that the portion of the (unknown) rate cross-section represented by the measured coherent one is of the order of about 90%. This result may be of help to experimentalists as an additional criterion in deciding to employ molybdenum as a detector in neutral-current neutrino–nucleus measurements.

Table 1. Coherent, incoherent and total differential cross-sections (in units of 10^{-42} MeV^{-1} cm ^{2}) of neutrino scattering off the ^{94,96,98,100}Mo detector isotopes. The portion of the coherent into the total cross-section is also listed. The results for ^{98,100}Mo are first reported in [19] and for ^{96}Mo in [18].

Isotope	Coherent	Incoherent	Total	Coherent/Total (%)
^{94}Mo	1165.0	150.4	1315.4	88.56 (%)
^{96}Mo	1338.5	230.0	1568.5	85.34 (%)
^{98}Mo	1506.2	147.7	1653.9	91.07 (%)
^{100}Mo	1692.9	290.0	1982.9	85.38 (%)

6. Conclusions

In this work, we present predictions for the neutral-current ν–nucleus cross-sections both for the coherent and the incoherent channel assuming a Mo detector medium and employing the deformed shell model for some stable Mo isotopes. As it is known, molybdenum has seven stable isotopes with abundances as follows: ^{92}Mo (15.86%), ^{94}Mo (9.12%), ^{95}Mo (15.70%), ^{96}Mo (16.50%), ^{97}Mo (9.45%), ^{98}Mo (23.75%), and ^{100}Mo (9.62%). Molybdenum as a neutrino-detector material has been employed by the MOON neutrino and double-beta decay experiment but also by the NEMO neutrinoless double-beta decay experiment.

In our previous calculation, restricted to ^{98,100}Mo, we have not included the contributions in the CEνNS cross-sections stemming from the stable ^{94,96}Mo isotopes, and in this work, we presented detailed coherent and incoherent ν-^{94,96}Mo cross-sections for which there are no previous CEνNS cross-section results. We have, in addition, obtained values for the Coherent/(Coherent + Incoherent) ratio, which is of great interest for experimentalists, since it represents the portion of the measured event rate over the total one.

For our cross-sections calculations in this work, we utilized the Donnelly–Walecka multipole decomposition method in which the ν–nucleus cross-sections are computed state-by-state as a function of the excitation energy of the target nucleus (or the outgoing neutrino energy). The nuclear excitation spectrum for each of the Mo isotopes studied is derived within the context of the deformed shell model that has been previously employed in the study of many electroweak interaction processes.

In the great number of operating and designed CEνNS current experiments, only the coherent cross-section is measured via the recoil energy deposition on the detector

material that operates as the detection signal. In these experiments, several neutrino (or antineutrino) sources use pion decay-at-rest neutrinos, reactor neutrinos, etc.

In future calculations, we plan to perform similar cross-sections calculations for the rest of the stable Mo isotopes (i.e., for ^{92}Mo, ^{95}Mo and ^{97}Mo). Given the CEνNS cross-sections for all seven stable isotopes, one may easily find the events predicted to be measured by, for example, a Mo detector of 100 kg mass.

Author Contributions: Methodology, T.S.K. and R.S.; Validation, V.K.B.K.; Formal analysis, R.S.; Investigation, R.S. and V.K.B.K.; Data curation, R.S.; Writing – original draft, T.S.K., R.S. and V.K.B.K.; Supervision, T.S.K. and V.K.B.K. All the authors contributed equally. All authors have read and agreed to the published version of the manuscript.

Funding: This research was funded by the Association for Advancement of Research on Open Problems (OPRA Association, Tel Aviv, Israel) in Nuclear Physics & Particle Physics, project No 83241/ELKE-UoI, and also by SERB in the Department of Science and Technology (Government of India).

Data Availability Statement: All the numerical data for generating figures and tables of the paper can be obtained from the author, R. Sahu.

Acknowledgments: Thanks are due to P.C. Srivastava for some useful correspondence.

Conflicts of Interest: The authors declare no conflicts of interest.

References

1. Freedman, D.Z. Coherent effects of a weak neutral current. *Phys. Rev. D* **1974**, *9*, 1389. [CrossRef]
2. Scholberg, K. Prospects for measuring coherent neutrino–nucleus elastic scattering at a stopped-pion neutrino source. *Phys. Rev. D* **2006**, *73*, 033005. [CrossRef]
3. Kosmas, T.S.; Oset, E. Charged current neutrino-nucleus reaction cross sections at intermediate energies. *Phys. Rev. C* **1996**, *53*, 1409. [CrossRef]
4. Tsakstara, V.; Kosmas, T.S. Analyzing astrophysical neutrino signals using realistic nuclear structure calculations and the convolution procedure. *Phys. Rev. C* **2011**, *84*, 064620. [CrossRef]
5. Papoulias, D.K.; Kosmas, T.S. COHERENT constraints to conventional and exotic neutrino physics. *Phys. Rev. D* **2018**, *97*, 033003. [CrossRef]
6. Akimov, D.; Albert, J.B.; An, P.; Awe, C.; Barbeau, P.S.; Becker, B.; Belov, V.; Brown, A.; Bolozdynya, A.; Cabrera-Palmer, B.; et al. Observation of Coherent Elastic Neutrino-Nucleus Scattering. *Science* **2017**, *357*, 1123. [CrossRef]
7. Akimov, D.; An, P.; Awe, C.; Barbeau, P.S.; Becker, B.; Belov, V.; Bernardi, I.; Blackston, M.A.; Bock, C.; Bolozdynya, A.; et al. Measurement of the Coherent Elastic Neutrino-Nucleus Scattering Cross Section on CsI by COHERENT. *Phys. Rev. Lett.* **2022**, *129*, 081801. [CrossRef]
8. Akimov, D.; Albert, J.B.; An P.; Awe, C.; Barbeau, P.S.; Becker, B.; Belov, V.; Bernardi, I.; Blackston, M.A.; Blokland, L.; et al. First Measurement of Coherent Elastic Neutrino-Nucleus Scattering on Argon. *Phys. Rev. Lett.* **2021**, *126*, 012002. [CrossRef]
9. Colaresi, J.; Collar, J.; Hossbach, T.; Lewis, C.; Yocum, K. Measurement of Coherent Elastic Neutrino-Nucleus Scattering from Reactor Antineutrinos. *Phys. Rev. Lett.* **2022**, *129*, 211802. [CrossRef]
10. CONNIE Collaboration; Aguilar-Arevalo, A.; Bernal, J.; Bertou, X.; Bonifazi, C.; Cancelo, G.; de Carvalho, V.G.P.B.; Cervantes Vergara, B.A.; Chavez, C.; Corrêa, G.C.; et al. Search for coherent elastic neutrino-nucleus scattering at a nuclear reactor with CONNIE2019data. *J. High Energy Phys.* **2022**, *05*, 017.
11. Bonet, H.; Bonhomme, A.; Buck, C.; Fülber, K.; Hakenmüller, J.; Heusser, G.; Hugle, T.; Lindner, M.; Maneschg, W.; Rink, T.; et al. Novel constraints on neutrino physics beyond the standard model from the CONUS experiment. *J. High Energy Phys.* **2022**, *05*, 085.
12. Alekseev, I.; Balej, K.; Belov, V.; Evseev, S.; Filosofov, D.; Fomina, M.; Hons, Z.; Karaivanov, D.; Kazartsev, S.; Khushvaktov, J.; et al. First results of the νGeN experiment on coherent elastic neutrino-nucleus scattering. *Phys. Rev. D* **2022**, *106*, L051101. [CrossRef]
13. Agnolet, G.; Baker, W.; Barker, D.; Beck, R.; Carroll, T.J.; Cesar, J.; Cushman, P.; Dent, J.B.; Rijck, S.D.; Dutta, B.; et al. Background Studies for the MINER Coherent Neutrino Scattering Reactor Experiment. *Nucl. Instrum. Meth. A* **2017**, *853*, 53. [CrossRef]
14. Billard, J.; Carr, R.; Dawson, J.; Figueroa-Feliciano, E.; Formaggio, J.A.; Gascon, J.; Jesus, M.D.; Johnston, J.; Lasserre, T.; Leder, A.; et al. Coherent Neutrino Scattering with Low Temperature Bolometers at Chooz Reactor Complex. *J. Phys. G* **2017**, *44*, 105101. [CrossRef]
15. Strauss, R.; Rothe, J.; Angloher, G.; Bento, A.; Gütlein, A.; Hauff, D.; Kluck, H.; Mancuso, M.; Oberauer, L.; Petricca, F.; et al. The ν-cleus experiment: A gram-scale fiducial-volume cryogenic detector for the first detection of coherent neutrino-nucleus scattering. *Eur. Phys. J. C* **2017**, *77*, 506. [CrossRef]
16. Wong, H.T.-K. Taiwan EXperiment On NeutrinO—History and Prospects. *Universe* **2015**, *3*, 22–37. [CrossRef]

17. Augier, C.; Baulieu, G.; Belov, V.; Bergé, L.; Billard, J.; Bres, G.; Bret, J.-L.; Broniatowski, A.; Calvo, M.; Cazes, A.; et al. Results from a Prototype TES Detector for the Ricochet Experiment. *arXiv* **2023**, arXiv:2304.14926v1. [CrossRef]
18. Sahu, R.; Kota, V.K.B.; Kosmas, T.S. Deformed shell model applications to weak interaction processes. *Particles* **2024**, *7*, 595–602. [CrossRef]
19. Sahu, R.; Kota, V.K.B.; Kosmas, T.S. Cross sections of neutral-current neutrino scattering on ^{98,100}Mo isotopes. *J. Phys. G Nucl. Part. Phys.* **2024**, *51*, 065104. [CrossRef]
20. Kolbe, E.; Langanke, K.; Vogel, P. Estimates of weak and electromagnetic nuclear decay signatures for neutrino reactions in Super-Kamiokande. *Phys. Rev. D* **2002**, *66*, 013007. [CrossRef]
21. Balasi, K.G.; Ydrefors, E.; Kosmas. T.S. 2011 Theoretical study of neutrino scattering off the stable even Mo isotopes at low and intermediate energies. *Nucl. Phys. A* **2011**, *868–869*, 82–98. [CrossRef]
22. Ydrefors, E.; Mustonen, M.T.; Suhonen, J. MQPM description of the structure and beta decays of the odd A=95, 97 Mo and Tc isotopes. *Nucl. Phys. A* **2010**, 842, 33. [CrossRef]
23. Ydrefors, E.; Balasi, K.G,; Kosmas, T.S.; Suhonen, J. Detailed study of the neutral-current neutrino-nucleus scattering off the stable Mo isotopes. *Nucl. Phys. A* **2012**, 896, 1–23. [CrossRef]
24. Papoulias, D.; Hellgren, M.; Suhonen, J. Incoherent solar-neutrino scattering off the stable Tl-isotopes. *arXiv* **2024**, arXiv:2407.09889v1. [CrossRef]
25. Vergados, J.D.; Bonatsos, D. Theoretical WIMP–nucleus scattering rates for isomeric nuclei. *Particles* **2024**, 7, 810–817. [CrossRef]
26. The CRAB and NUCLEUS Collaborations: Observation of a nuclear recoil peak at the 100 eV scale induced by neutron capture. *Phys. Rev. Lett.* **2023**, *130*, 211802. [CrossRef]
27. Bonet, H.; Bonhomme, A.; Buck, C.; Fülber, K.; Hakenmüller, J.; Heusser, G.; Hugle, T.; Lindner, M.; Maneschg, W.; Rink, T.; et al. Constraints on Elastic Neutrino Nucleus Scattering in the Fully Coherent Regime from the CONUS Experiment. *Phys. Rev. Lett.* **2021**, *126*, 041804. [CrossRef]
28. Kota, V.K.B.; Sahu, R. *Structure of Medium Mass Nuclei: Deformed Shell Model and Spin-Isospin Interacting Boson Model*; CRC Press: Boca Raton, FL, USA, 2017.
29. Ejiri, H. Majorana neutrino masses by spectroscopic studies of double beta decays and MOON. *Mod. Phys. Lett. A* **2007**, *22*, 1277. [CrossRef]
30. Fushimi, K.; Kameda, Y.; Harada, K.; Nakayama, S.; Ejiri, H.; Shima, T.; Yasuda, K.; Hazama, R.; Imagawa, K. MOON for Double-Beta Decays and Neutrino Nuclear Responses. *J. Phys. Conf. Ser.* **2010**, *203*, 012064. [CrossRef]
31. Arnold, R.; Augier, C.; Baker, J.D. Results of the search for neutrinoless double-beta decay in 100Mo with the NEMO-3 experiment. *Phys. Rev. D* **2015**, *92*, 072011. [CrossRef]
32. Baxter, D.; Bloch, I.M.; Bodnia, E.; Chen, X.; Conrad, J.; Di Gangi, P.; Dobson, J.E.Y.; Durnford, D.; Haselschwardt, S.J.; Kaboth, A.; et al. Recommended conventions for reporting results from direct dark matter searches. *Eur. Phys. J. C* **2021**, 81, 907. [CrossRef]
33. An, F.P.; Balantekin, A.B.; Band, H.R.; Bishai, M.; Blyth, S.; Butorov, I.; Cao, D; Cao, G.F.; Cao, J.; Cen, W.R.; et al. Measurement of the Reactor Antineutrino Flux and Spectrum at Daya Bay. *Phys. Rev. Lett.* **2016**, 116, 061801. [CrossRef]
34. Vitagliano, E.; Tamborra, I.; Raffelt, G. Grand unified neutrino spectrum at Earth: Sources and spectral components. *Rev. Mod. Phys.* **2020**, 92, 045006. [CrossRef]
35. Donnelly, T.W.; Walecka, J.D. Semi-leptonic weak and electromagnetic interactions with nuclei: Isoelastic processes. *Nucl. Phys. A* **1976**, *274*, 368. [CrossRef]
36. Donnelly, T.W.; Peccei, R.D. Neutral current effects in nuclei. *Phys. Rep.* **1979**, *50*, 1. [CrossRef]
37. Tsakstara, V.; Kosmas, T.S. Low-energy neutral-current neutrino scattering on ^{128,130}Te isotopes. *Phys. Rev. C* **2011**, *83*, 054612. [CrossRef]
38. Chasioti, V. C.; Kosmas, T.S. A unified formalism for the basic nuclear matrix elements in semi-leptonic processes. *Nucl. Phys. A* **2009**, *829*, 234. [CrossRef]
39. Perdrisat, C.F.; Punjabi, V.; Vanderhaeghen, M. Nucleon Electromagnetic Form Factors. *Prog. Part. Nucl. Phys.* **2007**, *59*, 694. [CrossRef]
40. Dey, P.; Negi, D.; Palit, R.; Srivastava, P.C.; Laskar, M.S.R.; Das, B.; Babra, F.S.; Bhattacharya, S.; Das, B.; Devi, K.R.; et al. Experimental investigation of high-spin states in ^{90}Zr. *Phys. Rev. C* **2022**, *105*, 044307. [CrossRef]
41. Coraggio, L.; De Angelis, L.; Fukui, T.; Gargano, A.; Itaco, N. Calculation of Gamow-Teller and two-neutrino double-β decay properties for ^{130}Te and ^{136}Xe with a realistic nucleon-nucleon potential. *Phys. Rev. C* **2017**, *95*, 064324. [CrossRef]
42. National Nuclear Data Center. Available online: http://www.nndc.bnl.gov/ (accessed on 26 June 2024).